JACS
JOURNAL OF THE AMERICAN CHEMICAL SOCIETY
Article
pubs.acs.org/JACS

Influence of Confined Fluids on Nanoparticle-to-Surroundings Energy Transfer

Anne-Marie Dowgiallo and Kenneth L. Knappenberger, Jr.*

Department of Chemistry and Biochemistry, Florida State University, Tallahassee, Florida 32306-4309, United States

ABSTRACT: Energy transfer from photoexcited nanoparticles to their surroundings was studied for both hollow and solid gold nanospheres (HGNs and SGNs, respectively) using femtosecond time-resolved transient extinction spectroscopy. HGNs having outer diameters ranging from 17 to 78 nm and fluid-filled cavities were synthesized by a sacrificial galvanic replacement method. The HGNs exhibited energy transfer half times that ranged from 105 ± 10 ps to 1010 ± 80 ps as the total particle surface area increased from 1005 to 28 115 nm^2. These data showed behaviors that were categorized into two classes: energy transfer from HGNs to interior fluids that were confined to cavities with radii <15 nm and ≥15 nm. Energy transfer times were also determined for solid gold nanospheres (SGNs) having radii spanning 9−30 nm, with a similar size dependence where the relaxation times increased from 140 ± 10 to 310 ± 15 ps with increasing nanoparticle size. Analysis of the size-dependent energy transfer half times revealed that the distinct relaxation rate constants observed for particle-to-surroundings energy transfer for HGNs with small cavities were the result of reduced thermal conductivity of confined fluids. These data indicate that the thermal conductivity of HGN cavity-confined fluids is approximately one-half as great as it is for bulk liquid water. For all HGNs and SGNs studied, energy dissipation through the solvent and transfer across the particle/surroundings interface both contributed to the energy relaxation process. The current data illustrated the potential of fluid-filled hollow nanostructures to gain insight into the properties of confined fluids.

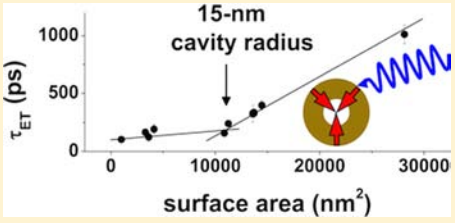

INTRODUCTION

Light-driven activation of metal nanostructures results in the formation of a nonequilibrium electron gas, which relaxes by three successive steps: (i) electron−electron scattering, (ii) electron−phonon coupling, and (iii) energy transfer to surroundings.[1] Ultrafast (∼100 fs) electron−electron (e−e) scattering forms a hot electron distribution that subsequently equilibrates with the metal lattice on a ∼1-ps time scale via electron−phonon (e−ph) coupling. The final step in this electronic energy relaxation sequence is energy transfer from the hot electron and phonon subsystems to the environment. This final particle-to-surroundings energy transfer process plays a critical role in determining the efficiency of many applications that feature metal nanostructures as functional hosts including micro/nanoelectronics,[2] material processing,[3] photodynamic therapy,[4] and electromagnetic energy transport through patterned nanoparticle networks.[5] The repertoire of nanostructure synthesis and fabrication techniques currently available allows for the production of particles over a vast range of sizes and morphologies, which can be exploited to tune particle-to-environment energy transfer rates.[6−11] Structure-dependent energy transfer rates can be quantified using femtosecond time-resolved transient extinction spectroscopy, which is a reliable experimental diagnostic for studying the rapid electronic energy relaxation mechanisms of metal nanostructures.[1,12−14]

The particle examined in the current study is the hollow gold nanosphere (HGN), which is composed of a gold shell and a fluid dielectric interior. HGNs are synthesized by a galvanic replacement method that permits control over the particle's outer-diameter-to-shell-thickness aspect ratio, yielding tunability of both the surface plasmon resonance (SPR) frequency and the total surface area of the nanostructure.[15] The latter structural parameter may provide a useful route for tailoring particle-to-environment relaxation rates of electronically excited gold nanostructures. However, the properties of the fluids confined to the nanoscale dimensions of the HGN interior cavity, and their influence on HGN optical, mechanical, and electronic relaxation properties, remain unclear. For example, cavity plasmon resonances appear to contribute significantly to interparticle modes that are formed when neighboring particles undergo near-field coupling.[16−18] HGNs also exhibit size-dependent electron−phonon equilibration rates; the electron−phonon coupling constant increases linearly with increasing particle surface-to-volume ratio.[19] This phenomenon is not observed for similarly sized solid gold nanospheres (SGNs). By comparison, electron−phonon coupling sensitivity to the surface-to-volume ratio does not occur for low-aspect-ratio HGNs, which exhibit electron−phonon coupling values comparable to SGNs. Aggregation of HGNs by surface necking results in decreased electron−phonon coupling rates owing to the formation of a continuous nanoparticle network that has a decreased effective surface-to-volume ratio.[16] In a separate but related study, we reported structure-dependent coherent acoustic oscillations of HGNs.[20] HGNs exhibit oscillations at frequencies lower than those observed for SGNs. Possible contributing factors include the increased lattice polycrystallinity of HGNs compared to SGNs as well as structure-dependent

Received: July 11, 2012
Published: October 30, 2012

energy dissipation for HGNs, which may be modified by the fluid-filled cavity.

Here, we report particle-to-surroundings energy transfer half times for a series of HGNs having outer diameter-to-shell thickness aspect ratios ranging from 3 to 9 and total surface areas ranging from 1.0×10^3 to 2.8×10^4 nm^2. The apparent energy transfer half times were obtained using femtosecond time-resolved pump−probe transient extinction spectroscopy. As the HGN surface area increased, the energy transfer half times also increased, but the data showed a discontinuity at a particle cavity radius of 15 nm. Analysis of HGN interfacial energy transfer indicated small HGNs (cavity radius <15 nm) had interfacial thermal conductivities that were ∼1.9−2.4 times less than those of SGNs and larger HGNs. This effect was attributed to the difference between the thermal conductivity of water confined to small HGN cavities and that for bulk water. The apparent energy transfer half times were also sensitive to the surrounding environment, becoming larger when the HGNs were dispersed in methanol, which has a lower thermal conductivity than water.

EXPERIMENTAL METHODS

Synthesis and Characterization of Gold Nanospheres. Hollow gold nanospheres were synthesized by a sacrificial galvanic replacement technique involving the oxidation of cobalt nanoparticles and the subsequent reduction of gold ions.[15] Under deoxygenated conditions and constant argon flow, cobalt nanoparticles were first synthesized by the sodium borohydride-mediated reduction of Co^{2+} ions in the presence of citrate ions. Once hydrogen gas formation had ceased, the desired amount of gold salt was added to the cobalt nanoparticle suspension where the Co^0 oxidized to Co^{2+} ions and Au^{3+} ions reduced to Au^0 onto the cobalt nanoparticle template. Exposure to ambient conditions ensured the complete oxidation of the cobalt nanoparticle and formation of a thin gold shell encapsulating water. Desired HGN aspect ratios were achieved by altering the relative amounts of citrate, $NaBH_4$, and $HAuCl_4$ injected into the reaction. SGNs were prepared by citrate reduction of gold, following the method reported by Ghosh et al.[21] For solvent-dependent studies, both HGNs and SGNs were transferred from water to methanol solutions. HGN and SGN solutions were subjected to centrifugation at 5000 rpm for 30 min. The aqueous supernatant was discarded, and the pellet was redispersed in methanol via sonication.

The resulting HGNs and SGNs were characterized by UV−vis absorption spectrophotometry (Perkin-Elmer Lambda 950) and transmission electron microscopy (FEI CM-120 TEM, 120-kV acceleration voltage). Samples were applied to a Formvar-coated copper grid and air-dried for 24 h prior to TEM image acquisition. TEM images were analyzed using ImageJ software to determine the HGN size distributions.

Femtosecond Time-Resolved Transient Extinction Spectroscopy. Femtosecond pump−probe transient extinction experiments were performed on a 1-kHz regeneratively amplified Ti:Sapphire laser system that delivered 800-μJ pulse energies centered at 800 nm. The duration of the amplified pulse was typically ∼90 fs, and the pulse was characterized by frequency-resolved optical gating pulse diagnostics.[22] The amplified laser output was frequency doubled to generate 400-nm light (200 μJ/pulse), which was attenuated and used as the excitation pump pulse. Excitation pulse energies used here ranged from 100 to 1.0 μJ/pulse. A small portion (4%) of the fundamental laser output was passed through a sapphire plate to generate the continuum probe pulse that typically extended from 450 to 850 nm. The pump−probe time delay was controlled using a retroreflecting mirror mounted on a motorized linear translation stage (Newport). Both pulses were spatially overlapped in the sample−laser interaction region. Differential extinction of the probe was measured as a function of the time delay between the pump and probe by mechanically chopping the pump pulse at 500 Hz. Here, the probe was spectrally dispersed on a silicon diode array to generate a wavelength-resolved differential extinction spectrum that spanned from 450 to 800 nm. Data were acquired for 2 s at each pump−probe delay. The instrument response time (∼150 fs) was determined from the nonresonant response of the pump and probe pulses in water. The full dynamic range of the measurements extended from 10 ps before to 3.2 ns after time zero. Data fitting used in this work was similar to previously published methods. Here, temporal integration of the SPR bleach measured in the transient extinction spectrum provided electronic relaxation kinetic traces. The transient data was fit with an in-house program that uses an iterative least-squares approach.[23,24] The best fits were obtained using a biexponential decay function, which accounted for both electron−phonon and phonon−phonon relaxation rates:

$$S(t) = \left[A_{\text{el-ph}} \exp\left(\frac{-t}{\tau_{\text{el-ph}}}\right) + A_{\text{ph-ph}} \exp\left(\frac{-t}{\tau_{\text{ET}}}\right)\right] \quad (1)$$

$A_{\text{el-ph}}$ and $A_{\text{ph-ph}}$ are amplitude coefficients that described the contributions from electron−phonon relaxation and nanoparticle-to-surroundings energy transfer, respectively, and $\tau_{\text{el-ph}}$ and τ_{ET} are the half times for electron−phonon relaxation and nanoparticle-to-surroundings energy transfer, respectively. The pump−probe delay time was given by t.

RESULTS AND DISCUSSION

In order to characterize the HGN optical properties and structure, extinction spectra (Figure 1) and TEM data (Figure 2) were collected. On the basis of the statistics obtained from TEM images of at least 200 particles for each HGN sample, our syntheses yielded particles with nine different outer diameter/shell thickness dimensions: (HGN-1) 16.6 ± 2.9 nm/5.0 ± 1.2 nm, (HGN-2) 29.9 ± 6.2 nm/8.5 ± 2.2 nm, (HGN-3) 27.9 ± 3.2 nm/6.3 ± 1.3 nm, (HGN-4) 31.2 ± 4.6 nm/6.3 ± 2.1 nm, (HGN-5) 48.0 ± 5.0 nm/7.0 ± 1.0 nm, (HGN-6) 51.1 ± 5.1 nm/10.0 ± 1.0 nm, (HGN-7) 53.2 ± 7.2 nm/7.1 ± 1.6 nm, (HGN-8) 52.2 ± 8.0 nm/5.9 ± 1.0 nm, and (HGN-9) 77.9 ± 5.5 nm/11.3 ± 2.2 nm. Their outer-diameter-to-shell-thickness aspect ratios were the following: 3.4 ± 0.6, 3.7 ± 0.6, 4.5 ± 0.7, 5.4 ± 1.5, 6.9 ± 1.7, 5.1 ± 0.6, 7.8 ± 1.6, 9.0 ± 1.6, and 6.9 ± 1.2, respectively. In addition, SGNs were examined that had outer diameters of (SGN-1) 18.3 ± 2.0 nm, (SGN-2) 25.4 ± 4.2 nm, (SGN-3) 38.4 ± 4.2 nm, and (SGN-4) 59.8 ± 7.8 nm. Particle size data for HGNs and SGNs are reported in Tables 1 and 2, respectively. The maximum wavelengths of the SPR

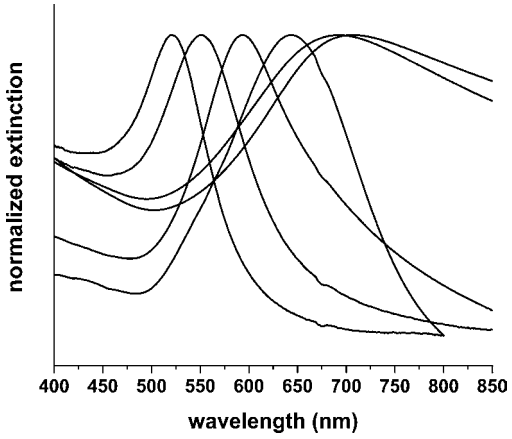

Figure 1. Normalized extinction spectra for select HGN samples used in this study. The SPR maximum wavelength ranges from 550 to 710 nm with increasing outer-diameter-to-shell-thickness aspect ratio.

dx.doi.org/10.1021/ja306644p | J. Am. Chem. Soc. 2012, 134, 19393−19400

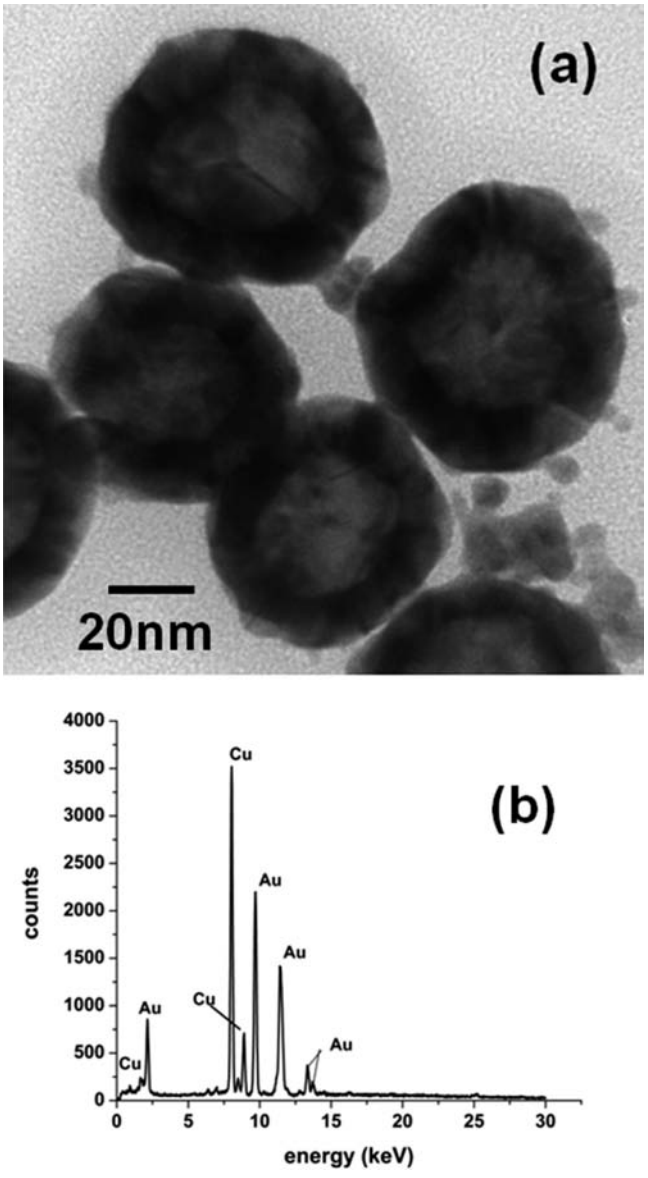

Figure 2. Representative TEM images of sample HGN-6 (a) and corresponding EDS data (b). The scale bar in part a is 20 nm. The images and EDS data indicated that the structures were composed of a gold shell and a hollow cavity. Cu peaks in panel b arose from the sample grid and were not indicative of sample contamination.

Table 1. Energy Transfer Half Times and Structural Parameters for Citrate-Stabilized HGNs

sample	outer diameter, shell thickness (nm)	surface area (nm^2)	$S:V$ (nm^{-1})	τ_{ET} (ps)
HGN-1	16.6 ± 2.9, 5.0 ± 1.2	1.00×10^3	0.45	105 ± 10
HGN-2	29.9 ± 6.2, 8.5 ± 2.2	3.34×10^3	0.26	165 ± 30
HGN-3	27.9 ± 3.2, 6.3 ± 1.3	3.17×10^3	0.33	155 ± 40
HGN-4	31.2 ± 4.6, 6.3 ± 2.1	4.13×10^3	0.33	195 ± 40
HGN-5	48.0 ± 5.0, 7.0 ± 1.0	1.09×10^4	0.29	160 ± 15
HGN-6	51.1 ± 5.1, 10.0 ± 1.0	1.13×10^4	0.21	245 ± 25
HGN-7	53.2 ± 7.2, 7.1 ± 1.6	1.36×10^4	0.29	325 ± 70
HGN-8	52.2 ± 8.0, 5.9 ± 1.0	1.37×10^4	0.34	330 ± 30
HGN-9	77.9 ± 5.5, 11.3 ± 2.2	2.86×10^4	0.18	1010 ± 80

responses for the HGNs ranged from 550 to 710 nm, with longer SPR wavelengths being observed for HGNs with larger

Table 2. Energy Transfer Half Times and Structural Parameters for Citrate-Stabilized SGNs

sample	outer diameter (nm)	surface area (nm^2)	$S:V$ (nm^{-1})	τ_{ET} (ps)
SGN-1	18.3 ± 2.0	1.05×10^3	0.33	140 ± 10
SGN-2	25.4 ± 4.2	2.03×10^3	0.24	170 ± 10
SGN-3	38.4 ± 4.2	4.64×10^3	0.16	210 ± 20
SGN-4	59.8 ± 7.8	1.12×10^4	0.10	310 ± 15

outer-diameter-to-shell-thickness aspect ratios. Representative transmission electron micrographs of HGN-6 are given in Figure 2. TEM images, along with energy dispersive analysis (Figure 2b), indicated that the HGNs consisted of a thin gold shell and a hollow cavity. Taken together, the optical and TEM data provided evidence that the solution-phase samples used for transient extinction spectroscopy measurements were gold shells with fluid-filled cavities; cavity radii ranged from 3.3 to 27.5 nm.

After the initial structural and optical characterization, time-resolved transient extinction experiments were performed to examine the relaxation dynamics of electronically excited HGNs and SGNs. Both HGNs and SGNs were excited using a 400-nm laser pulse, and the relaxation dynamics of the electron and phonon systems were subsequently probed using a continuum laser pulse. The transient extinction spectrum obtained from one sample (HGN-6) is shown in Figure 3a; the spectrum was recorded at a pump−probe delay of 5 ps, following excitation by a 500-nJ, 400-nm pump pulse. A broad transient bleach centered at 610 nm was observed, which was consistent with the λ_{max} of the sample's SPR band. Coincidence of the center wavelength of the transient bleach and the SPR maximum obtained from linear extinction measurements was observed for all samples studied.

The kinetics of electronic relaxation were determined by measuring the transient bleach recovery in the time domain. The cooling of sample HGN-6 is shown in Figure 3b. These time-resolved transient extinction traces depict the magnitude of the 610-nm signal as a function of the pump−probe time delay; data for all samples correspond to the center wavelength of the transient bleach in the time domain. Each HGN and SGN sample examined here yielded time-resolved transient data that exhibited two distinct components: (1) an initial, fast decay that was completed within ∼1 ps and (2) a slower decay that persisted for hundreds of picoseconds. The fast component 1 of this HGN relaxation process has been discussed previously.[19] These two distinct relaxation processes are also observed for large SGNs (>15-nm diameter).[25,26] Hartland and co-workers attribute the first component to coupling between the photoinduced hot electron system and lattice phonons of the particle.[25,26] They assign the second component to energy transfer as heat from the particle to the surroundings. The observation of a distinct transition from the fast to the slow component was important, because it indicated that the hot electrons equilibrated with the particle's phonon bath prior to energy transfer to the surroundings. Energy transfer did not compete with electron−phonon coupling for any of the HGNs studied here. Although competitive ET and e−ph coupling was observed for some smaller HGNs, those samples were not included in the current analysis. The experimental data shown in Figure 3b are plotted along with the fit results obtained using eq 1, which allowed for quantitative analysis of the structure-dependent energy dissipation half times. The dimensions of

dx.doi.org/10.1021/ja306644p | J. Am. Chem. Soc. 2012, 134, 19393−19400

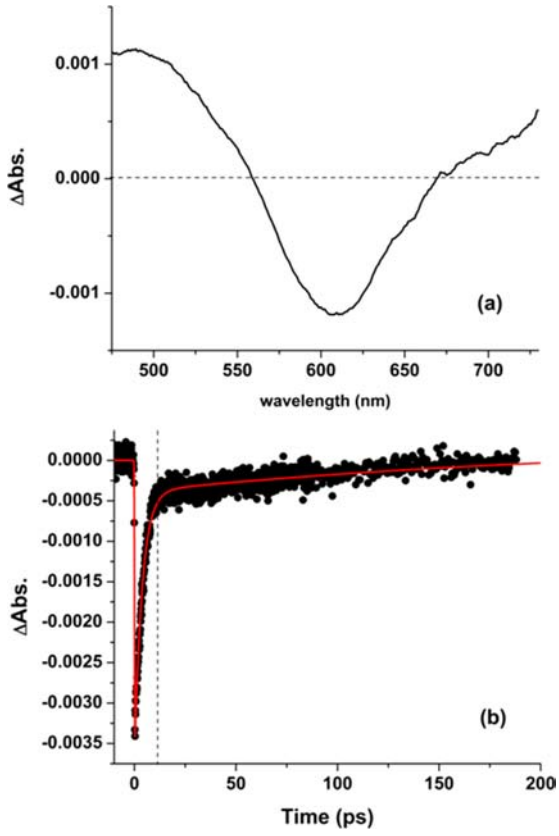

Figure 3. (a) Spectrally resolved transient extinction spectra of HGN-6. The data were recorded at a pump−probe time delay of 5 ps following excitation by a 400-nm laser pulse (500 nJ/pulse). (b) Temporally resolved extinction data obtained by monitoring the spectrum shown in panel a at a probe wavelength of 610 nm (center wavelength of bleach). The experimental data are plotted along with the best fit to the data, obtained using eq 1. The dashed vertical line in panel b provides a guide to the point at which the data reflect nanoparticle-to-surroundings energy transfer kinetics.

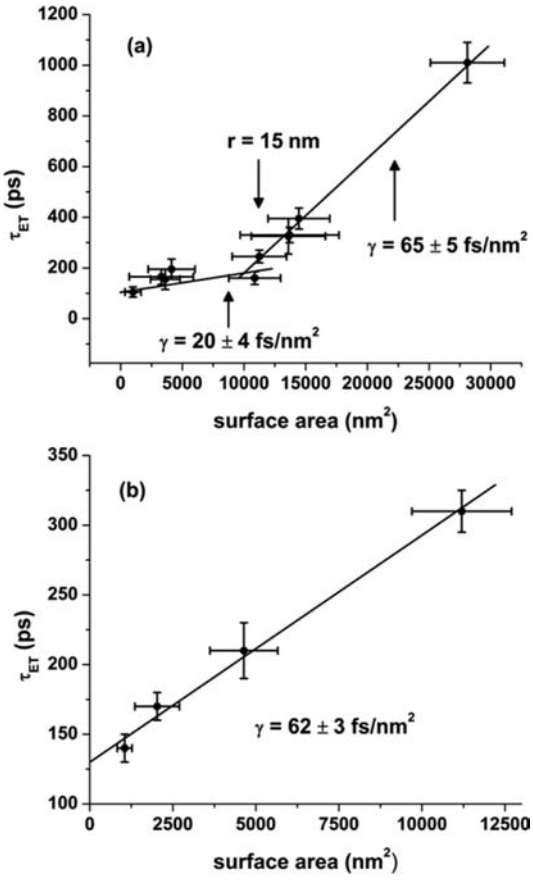

Figure 4. Nanoparticle-to-surroundings energy transfer half times (τ_{ET}) of HGNs plotted as a function of their total surface area. These HGNs have cavity radii ranging from 3.3 to 27.5 nm, shell thicknesses from 5 to 11 nm, and aspect ratios from 3 to 9. The data exhibited behaviors that were categorized in two classes: HGNs with cavity radii <15 nm and those with cavity radii ≥15 nm. The data point corresponding to a 15-nm HGN cavity radius is denoted by an arrow. In both cases, the τ_{ET} half time was linearly dependent on the total surface area. A linear fit to the data collected for HGNs with small cavities yielded $\gamma = 20 \pm 4$ fs/nm^2; $\gamma = 65 \pm 5$ fs/nm^2 was obtained for large cavities. *x*-Axis error bars were determined based on the outer and inner diameters from TEM images of several particles, and assume uniform HGN shells. (b) Nanoparticle-to-surroundings energy transfer half times of SGNs as a function of their total surface area. The τ_{ET} relaxation time is linearly dependent on the surface area, with a γ value of 62 ± 3 fs/nm^2.

each HGN sample and their respective energy transfer half times (τ_{ET}) are summarized in Table 1. Similar information is provided for the SGN samples in Table 2. Time-resolved transient extinction measurements were carried out in triplicate at several excitation pulse energies. The energy transfer half times were independent of laser power (unlike the electron−phonon coupling times); hence, the relaxation times obtained for different powers were averaged to determine the energy transfer half times for each sample.

In order to summarize size-dependent nanoparticle energy transfer, the time constants obtained for energy transfer from the photoexcited nanoparticles to the surroundings were plotted with respect to the total surface area for each of the nanoparticles. Figure 4a shows the energy-transfer-to-solvent half times for all of the HGN samples as a function of total surface areas. Two distinct regions of the plot were observed, both of which exhibited linear surface area dependencies for the energy transfer half times. HGNs with small surface areas resulted in a shallower slope. In addition, the shallow-sloped portion of Figure 4a corresponded to HGNs with cavity radii <15 nm, whereas the data for the HGNs with cavity radii ≥15 nm fell on the portion of Figure 4a characterized by the steeper slope. A linear dependence of the energy transfer time constants upon the surface area was also observed for the SGN samples (Figure 4b). As established by Hartland, the slope of the linear relationship between τ_{ET} and the particle's total surface area is γ (sec/nm^2), or the time constant of energy transfer per unit surface area.[26] A linear fit to the data in Figure 4a yielded $\gamma = 20 \pm 4$ fs/nm^2 for HGNs with cavity radii <15 nm, and $\gamma = 65 \pm 5$ fs/nm^2 for HGNs with cavity radii ≥15 nm. The same analysis resulted in $\gamma = 62 \pm 3$ fs/nm^2 for SGNs, in agreement with previous studies.[26] These data showed that HGNs with large cavities (radii ≥15 nm) transferred energy at a rate comparable to that observed for SGNs. In contrast, HGNs in which the interior fluid was confined to small (<15-nm radii) cavities exhibited energy transfer rates that differed from SGNs and larger HGNs by a factor of ∼3.1−3.3.

In order to understand the origin of the discontinuity observed at $r = 15$ nm in the energy transfer time constants of HGNs, it is necessary to consider all possible contributing mechanisms: (1) energy transfer across the nanoparticle/surroundings interface and (2) heat dissipation through the

dx.doi.org/10.1021/ja306644p | J. Am. Chem. Soc. 2012, 134, 19393−19400

surroundings. If energy transfer across the interface were the rate-limiting step, the energy transfer time constants would be expected to scale linearly with the particle's surface-to-volume ratio.[27] On the other hand, if heat dissipation through the solvent were limiting, the relaxation time constants would be expected to scale linearly with the particle's surface area.[27] For systems in which the particle-to-surroundings energy transfer is limited by diffusion through the surroundings, the heat dissipation half times (τ_d) depend on the surface area (SA) of the particle and the thermal conductivity (Λ_s), density (ρ_s), and heat capacity (C_s) of the surroundings as follows:

$$\tau_d = \frac{SA}{\sqrt{\Lambda_s \rho_s C_s}} \quad (2)$$

The data shown in Figure 4, which showed a linear dependence of the energy transfer time constant on both HGN and SGN total surface areas, identify heat diffusion within the surroundings of the nanoparticle as an important component in the relaxation process. However, the fact that none of the data in Figure 4 included a value of zero for the *y*-axis intercept indicated that eq 2 did not fully account for the data. Therefore, energy transfer across the metal/surroundings interface was included in the data analysis.

The time required for energy transfer across the nanoparticle interface (τ_i) increases as a linear function of SGN radius (HGN shell thickness; $R - r$) and the particle's volumetric heat capacity (C_p). The interfacial energy transfer time is inversely dependent upon interfacial thermal conductivity, G:

$$\tau_i = \frac{(R - r)C_p}{3G} \quad (3)$$

Eq 3 describes interfacial energy transfer for HGNs; for SGNs ($R - r$) is replaced by r. Interface effects become significant when τ_d and τ_i are comparable. As such, a critical value for G, which reflects the onset of interfacial contributions to the relaxation dynamics, can be obtained by equating eqs 2 and 3.[27,28]

$$G_{critical} = \frac{3C_f\Lambda_f}{(R - r)C_p} \quad (4)$$

When G greatly exceeds $G_{critical}$, energy diffusion through the solvent dominates heat dissipation by excited nanoparticles. Eq 4 was used to calculate the critical interface thermal conductance for the HGNs studied here. The resultant values of $G_{critical}$ spanned from ~265 to ~600 MW/m^2 K. C_f is the heat capacity of the fluid and Λ_f is the thermal conductivity of the fluid. Previous studies on SGNs in water yielded G = 100−110 MW/m^2 K.[1,29,30] Taken together, our calculations and previous experimental results indicated interfacial energy transfer must be included in the analysis of the relaxation dynamics for all HGN samples. Importantly, since $G_{critical} > G$ for all HGNs, the discontinuity observed in Figure 4a did not result from a size-dependent crossover from interface- to diffusion-controlled nanoparticle-to-surroundings energy transfer.

Interfacial conductivity was estimated by plotting the experimentally determined energy transfer half times with respect to HGN shell thickness and SGN radius (Figure 5). These data were fit to eq 3 to obtain G. In the case of SGNs, analysis of our experimental data resulted in G = 85 MW/m^2 K, which provided good agreement with previous research.[1,29,30]

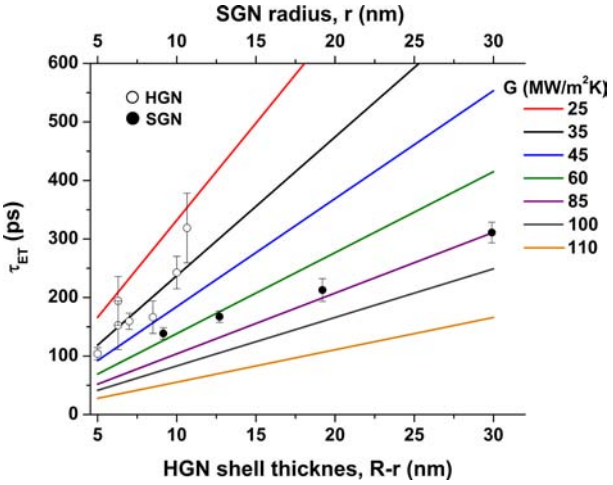

Figure 5. HGN (○) and SGN (●) energy transfer half times (τ_{ET}) plotted as a function of HGN shell thickness, or SGN radius. The experimental half times are plotted along with calculated size-dependent interfacial thermal conductivities, G. The values for G were obtained using eq 3, and bulk values obtained from ref 31.

However, the interfacial thermal conductance obtained for HGNs ranged from G = 35 to G = 45 MW/m^2 K, which was significantly reduced compared to SGNs. These data represented a reduction in interfacial thermal conductance by a factor of ~1.9−2.4, which indicated that the thermal conductivity (Λ_s) of confined water is less than that of bulk water. We do note that the experimental data provides an estimate of Λ_s, on the basis of the assumption that interfacial conductance was the rate-limiting step (i.e., $G_{critical} > G$). The data indicated that heat diffusion through the fluid also contributed to the relaxation dynamics.

The fluid thermal conductivity is related to the experimentally determined interfacial conductance as $G = \Lambda/h$, where h is the thickness of the solvent layer required to dissipate the energy transferred across the nanoparticle/fluid interface.[28] The thermal conductivity of liquid water is 0.6 W/mK.[31] Our experimental value for G from SGNs (85 MW m^{-2} K^{-1}) implies h ~7 nm. Assuming energy transfer through 7 nm of cavity-confined water, the thermal conductivities obtained for the HGNs (G = 35−45 MW m^{-2} K^{-1}) indicate Λ = 0.25−0.31 W m^{-1} K^{-1}. These data imply the thermal conductivity of cavity-confined fluids are ~1.9−2.4 times less than that of bulk water. We note that the nature of the cavity interface is not well understood. Citrate ions were used to passivate the HGN surface. These ions have a molecular diameter of 0.6 nm,[11] which may limit, but not prohibit, their diffusion to the cavity during the galvanic replacement process. Nonetheless, we assume the outer HGN surface is more completely passivated than the cavity. As a result cavity-confined fluids can more readily access the metal surface. Previous studies focused on the influence of capping agent concentration on interface thermal conductivity.[29] These results show that lower capping agent concentration increases, not decreases, the value of G. This effect occurs because incomplete surface passivation allows water molecules access to the nanoparticle surface, resulting in increased thermal conductivity of the interface. Therefore, the reduced G that we observed for HGNs with cavity radii <15 nm reflected differences between the thermal conductivity of bulk and cavity-confined fluids, rather than incomplete passivation of the nanoparticle cavity surface by the capping agent. As such,

dx.doi.org/10.1021/ja306644p | J. Am. Chem. Soc. 2012, 134, 19393−19400

the G values should have reflected the properties of the cavity fluids, although some energy transfer to water at the outer surface could also have contributed to the relaxation dynamics.

Previous computational studies also show that the thermal conductivity of water that is restricted to nanoscale dimensions can be distinct from that of bulk water.[32] In addition, the low-frequency vibrational modes of water shift to higher energies when water is confined to nanometer-sized pools, which range from 1.5 to 9.0 nm in radius.[33] These changes result in a decrease in the effective heat capacity upon going from bulk to confined water. Although more research is necessary to understand the properties of the water confined to small HGN cavities, the current time-domain data clearly indicated that the thermal conductivities of these fluids were ∼1.9−2.4 times less than that observed for bulk water. This apparent step function in the thermal properties of water must have its break around 15 nm because HGNs with cavity radii ≥15 nm were characterized by similar properties as those observed for bulk water.

The kinetic traces obtained for nanoparticle-to-surroundings energy transfer were fit using a single time constant for eight of the nine HGNs studied. The ability of a single-exponential function to describe the energy relaxation data for most of the HGNs indicated that the cavity-confined water was the reservoir for nanoparticle energy transfer; largely unrestricted access of water to the cavity surface favored energy transfer to the interior fluid. By comparison, the data obtained for the largest HGN (HGN-9) required a second exponential, yielding time constants of 110 ± 10 and 1010 ± 80 ps (Figure 6). The

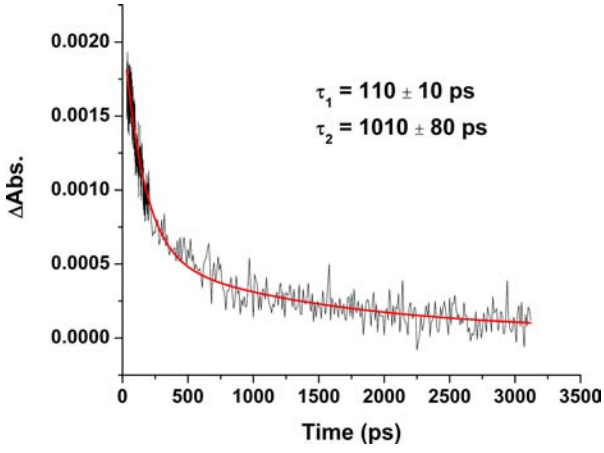

Figure 6. Nanoparticle-to-surroundings energy transfer relaxation kinetics obtained for HGN-9. The raw differential absorption data (black) is plotted along with the result from a two-component exponential decay (red). The bleach data was inverted for clarity.

fast time constant was comparable to the value obtained for an HGN with a 3.5-nm cavity radius. The HGN lattice can be porous, having pinholes of 1−2 nm in diameter.[34] These pinholes likely accommodate some water molecules, which serve as a low-temperature sink for energy transfer from hot HGNs.

In order to test further the nature of the nanoparticle energy relaxation process, the influence of the dispersing medium on the energy transfer from the particle to the surroundings was also determined. The time-resolved transient bleach data obtained for one SGN sample (20-nm radius) dispersed in both water and methanol are compared in Figure 7. It was

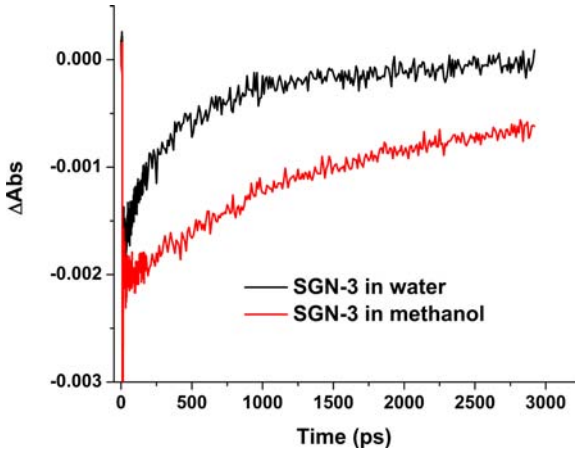

Figure 7. Comparison of the time-resolved extinctions obtained for SGN-3 dispersed in water (black trace) and methanol (red trace). The raw data reflected a slower transient bleach recovery for gold nanospheres dispersed in methanol than for those dispersed in water.

clearly evident that the energy transfer rate slowed down when the dispersion medium of the nanosphere was changed from water to methanol. This effect was also observed for HGN samples. For example, HGN-7 displayed an energy transfer time constant of 325 ± 70 ps in water; this value changed to 590 ± 60 ps in methanol. Similar results were obtained for HGN-8 (330 ± 30 ps in water; 600 ± 50 ps in methanol). By comparison, the energy transfer time constants of HGN-6 were 245 ± 25 ps in water and 600 ± 35 ps in methanol. In these three samples, the energy transfer time constants increased, on average, by a factor of ∼2.1 when the dispersion medium was altered from water to methanol. The energy transfer time constants obtained for HGN-6 in both water and methanol, using several excitation pulse energies, are depicted in Figure 8a. The ratio of the bulk thermal conductivities ($\Lambda_{H2O}/\Lambda_{CH3OH}$) is 3.[31] Therefore, the energy transfer time constants of HGNs and SGNs were expected to increase by a factor of 3 when methanol was used as the dispersing medium instead of water. The same solvent-dependent analysis was carried out for SGN samples (Figure 8b). In all cases the energy transfer time constant increased by a factor of 3 when the samples were dispersed in methanol instead of water, as expected on the basis of bulk thermal conductivities. These results were consistent with another study on SGNs:[35] for 15-nm SGNs, changing the surrounding matrix from an aqueous solution to an organic gel leads to a large increase in the phonon−phonon coupling time constant. This increase is also attributed to the lower thermal conductivity of the gel compared to that of water, which results in less efficient heat transfer from the particles to the surrounding matrix.[35] The size- and solvent-dependent kinetics of nanoparticle-to-surroundings energy dissipation observed for HGNs, which were distinct from those noted for SGNs, indicated that the properties of both cavity-confined water and methanol are different from those of bulk fluids. Therefore, HGNs provide a novel platform for investigating the properties of confined fluids.

Taken together, the size- and solvent-dependent energy relaxation time constants obtained here for HGNs indicated that heat diffusion within the surroundings and energy transfer across the nanoparticle/surroundings interface were both important processes mediating particle-to-surroundings energy transfer in both HGNs and SGNs. Hence, the discontinuity in

dx.doi.org/10.1021/ja306644p | J. Am. Chem. Soc. 2012, 134, 19393−19400

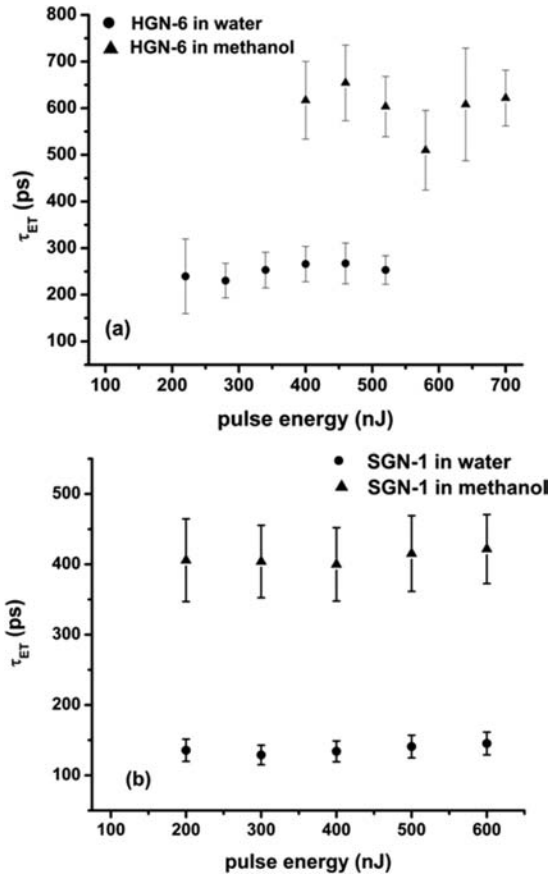

Figure 8. (a) Summary of the energy transfer half times obtained for HGN-6 dispersed in water or methanol at several excitation pulse energies. The data reflected an increase of τ_{ET} by a factor of ~2.5. (b) Summary of τ_{ET} for SGN-1 dispersed in methanol or water at several excitation pulse energies. The data reflected a 3-fold increase in the energy transfer half time.

energy relaxation time constants observed for HGNs that had cavity radii <15 nm was due to the fluid interior of the HGNs, which functions as a reservoir to which the particles supply energy.

CONCLUSIONS

Nanoparticle-to-surroundings energy transfer was studied for citrate-stabilized hollow and solid gold nanospheres with outer diameters ranging from 17 to 78 nm using femtosecond time-resolved transient extinction spectroscopy. The HGNs had fluid-filled cavities with radii ranging from 3 to 27.5 nm. In all cases, energy transfer across the nanoparticle/fluid interface and heat diffusion through the surroundings were both contributing energy relaxation mechanisms. The energy transfer half times ranged from 105 ± 10 ps to 1010 ± 80 ps for the HGNs and 140 ± 10 ps to 310 ± 15 ps for the SGNs. The data obtained for the preferential energy transfer from hot HGNs to cavity-confined fluids indicated that the HGNs could be split into two classes: those with cavity radii <15 nm and those with cavity radii ≥15 nm. In the former case, the kinetic data reflected an ~3-fold reduction in the thermal conductivities of confined water with respect to bulk values. In the latter case, HGN and SGN kinetics were similar, indicating that the thermal properties of water confined to cavities with radii ≥15 nm approached bulk values. Experiments on HGNs and SGNs dispersed in methanol also supported the idea that fluids confined to nanoscale dimensions (radius <15 nm) had different thermal properties than those observed for bulk fluids. In contrast, solvent-dependent data obtained for SGNs were consistent with predications based on bulk thermal conductivities. These data indicated that hollow nanostructures are useful for understanding the properties of fluids confined to nanoscale dimensions.

AUTHOR INFORMATION

Corresponding Author

klk@chem.fsu.edu

Notes

The authors declare no competing financial interest.

ACKNOWLEDGMENTS

This material is based upon work supported by the U.S. Air Force Office of Scientific Research under AFOSR Award FA9550-10-1-0300.

REFERENCES

(1) Hartland, G. V. *Chem. Rev.* **2011**, *111*, 3858−3887.
(2) Jacob, Z.; Shalaev, V. M. *Science* **2011**, *334*, 463−464.
(3) Dai, Z.; King, W. P.; Park, K. *Nanotechnology* **2009**, *20*, 095301.
(4) Hirsch, L. R.; Stafford, R. J.; Bankson, J. A.; Sershen, S. R.; Rivera, B.; Price, R. E.; Hazle, J. D.; Halas, N. J.; West, J. L. *Proc. Natl. Acad. Sci. U.S.A.* **2003**, *100*, 13540−13554.
(5) Feigenbaum, E.; Atwater, H. A. *Phys. Rev. Lett.* **2010**, *104*, 147402.
(6) Oldenburg, S. J.; Averitt, R. D.; Westcott, S. L.; Halas, N. J. *Chem. Phys. Lett.* **1998**, *288*, 243−247.
(7) Sau, T. K.; Murphy, C. J. *J. Am. Chem. Soc.* **2004**, *126*, 8648−8649.
(8) Chen, J.; Saeki, F.; Wiley, B. J.; Cang, H.; Cobb, M. J.; Li, Z. Y.; Au, L.; Zhang, H.; Kimmey, M. B.; Li, X.; Xia, Y. *Nano Lett.* **2005**, *5*, 473−477.
(9) Wang, H.; Brandl, D. W.; Nordlander, P. D.; Halas, N. J. *Nano Lett.* **2006**, *6*, 827−832.
(10) Kumar, P. S.; Pastoiza-Santos, I.; Rodriguez-Gonzalez, B.; Garcia de Abajo, F. J.; Liz-Marzan, L. M. *Nanotechnology* **2008**, *19*, 015606(1−6).
(11) Daniel, M. C.; Astruc, D. *Chem. Rev.* **2004**, *104*, 293−346.
(12) Hartland, G. V. *Phys. Chem. Chem. Phys.* **2004**, *6*, 5263−5274.
(13) Hartland, G. V. *Annu. Rev. Phys. Chem.* **2006**, *57*, 403−430.
(14) Del Fatti, N.; Flytzanis, C.; Vallée, F. *Appl. Phys. B: Lasers Opt.* **1999**, *68*, 433−437.
(15) Schwartzberg, A. M.; Olson, T. Y.; Talley, C. E.; Zhang, J. Z. *J. Phys. Chem. B* **2006**, *110*, 19935−19944.
(16) Knappenberger, K. L., Jr.; Schwartzberg, A. M.; Dowgiallo, A. M; Lowman, C. A. *J. Am. Chem. Soc.* **2009**, *131*, 13892−13893.
(17) Chandra, M.; Dowgiallo, A. M.; Knappenberger, K. L., Jr. *J. Am. Chem. Soc.* **2010**, *132*, 15782−15789.
(18) Chandra, M.; Dowgiallo, A. M.; Knappenberger, K. L., Jr. *J. Phys. Chem. C* **2010**, *114*, 19971−19978.
(19) Dowgiallo, A. M.; Knappenberger, K. L., Jr. *Phys. Chem. Chem. Phys.* **2011**, *13*, 21585−21592.
(20) Dowgiallo, A. M.; Schwartzberg, A. M.; Knappenberger, K. L., Jr. *Nano Lett.* **2011**, *11*, 3258−3262.
(21) Ghosh, S. K.; Pal, A.; Kundu, S.; Nath, S.; Pal, T. *Chem. Phys. Lett.* **2004**, *395*, 366−372.
(22) Kane, D. J.; Trebino, R. *IEEE J. Quantum Electron.* **1993**, *29*, 571.
(23) Attar, A. R.; Blumling, D. E.; Knappenberger, K. L., Jr. *J. Chem. Phys.* **2011**, *134*, 024514.
(24) Green, T. D.; Knappenberger, K. L., Jr. *Nanoscale* **2012**, *4*, 4111−4118.
(25) Hu, M.; Hartland, G. V. *J. Phys. Chem. B* **2002**, *106*, 7029−7033; **2003**, *107*, 1284.

(26) Hu, M.; Wang, X.; Hartland, G. V.; Salgueirino-Maceira, V.; Liz-Marzan, L. M. *Chem. Phys. Lett.* **2003**, *372*, 767−772.
(27) Wilson, O. M.; Hu., X.; Cahill, D. G.; Braun, P. V. *Phys. Rev. B* **2002**, *66*, 224301.
(28) Ge, Z.; Cahill, D. G.; Braun, P. V. *J. Phys. Chem. B* **2004**, *108*, 18870−18875.
(29) Schmidt, A. J.; Alper, J. D.; Chiesa, M.; Chen, G.; Das, S. K.; Hamad-Schifferli, K. *J. Phys. Chem. C* **2008**, *112*, 13320−13323.
(30) Plech, A.; Kotaidis, V.; Gresillon, S.; Dahmen, S.; von Plessen, G. *Phys. Rev. B* **2004**, *70*, 195423.
(31) *CRC Handbook of Chemistry and Physics*, 92nd ed.; CRC Press: Boca Raton, FL, 2011−2012; pp 6−242.
(32) Hu, M.; Goicochea, J. V.; Bruno, M.; Poulikakos, D. *Nano Lett.* **2010**, *10*, 279−285.
(33) Boyd, J. E.; Briksman, A.; Colvin, V. L. *Phys. Rev. Lett.* **2001**, *87*, 147401.
(34) Stagg, S. M.; Knappenberger, K. L., Jr.; Dowgiallo, A. M.; Chandra, M. *J. Phys. Chem. Lett.* **2011**, *2*, 2946−2950.
(35) Mohamed, M. B.; Ahmadi, T. S.; Link, S.; Braun, M.; El-Sayed, M. A. *Chem. Phys. Lett.* **2001**, *343*, 55−63.